

See discussions, stats, and author profiles for this publication at: <https://www.researchgate.net/publication/231390806>

Multiobjective Optimization of a Porous Ceramic Membrane Reactor for Oxidative Coupling of Methane

ARTICLE *in* INDUSTRIAL & ENGINEERING CHEMISTRY RESEARCH · JUNE 2010

Impact Factor: 2.59 · DOI: 10.1021/ie900971p

CITATIONS

5

READS

28

3 AUTHORS:



[Mohammad Rezwanul Quddus](#)

The University of Western Ontario

13 PUBLICATIONS 46 CITATIONS

SEE PROFILE



[Yan Zhang](#)

Memorial University of Newfoundland

27 PUBLICATIONS 222 CITATIONS

SEE PROFILE



[Ajay Ray](#)

The University of Western Ontario

175 PUBLICATIONS 4,995 CITATIONS

SEE PROFILE

Multiobjective Optimization of a Porous Ceramic Membrane Reactor for Oxidative Coupling of Methane

Mohammad R. Quddus, Yan Zhang, and Ajay K. Ray*

Department of Chemical and Biochemical Engineering, University of Western Ontario,
London, Ontario, Canada N6A 5B9

Multiobjective optimization of a porous ceramic membrane reactor for oxidative coupling of methane has been studied with the elitist nondominated sorting genetic algorithm with jumping genes (NSGA-II-aJG). A mathematical model was first developed and “tuned” using some experimental results available in the literature. A parametric sensitivity analysis was carried out on the experimentally verified model to systematically investigate the effects of the process parameters on the performance of the membrane reactor. Several two objective optimization problems were performed at both operating and design stages using NSGA-II-aJG. Significant performance improvement in terms of C₂ yield and selectivity could be achieved when rigorous optimization was performed.

1. Introduction

Catalytic oxidative coupling of methane (OCM) into valuable ethane and ethylene ($2\text{CH}_4 + 0.5\text{O}_2 \rightarrow \text{C}_2\text{H}_6 + \text{H}_2\text{O}$; $2\text{CH}_4 + \text{O}_2 \rightarrow \text{C}_2\text{H}_4 + 2\text{H}_2\text{O}$) offers a potential economical route and a great alternative for the conversion of the most abundant component of natural gas. As a result, this direct conversion of methane into higher hydrocarbons has been intensively studied compared to the indirect conversion technologies that need the energy-intensive step of syngas formation. However, thermodynamically favored deep oxidation of methane and C₂ products (ethane and ethylene) to carbon dioxide and water was the hurdle against achieving a yield of more than 25% in conventional co-feed fixed-bed reactors.^{1,2} Therefore, to achieve an economically attractive C₂ yield (30–40%) for the process to be commercially feasible, all endeavors toward the development of a more selective and active catalyst in the past two decades have thus been relocated to the development of different oxygen feed methods in several new types of reactors based on the concept of controlled oxygen concentration in order to prevent deep oxidation of desirable C₂ products, thereby increasing the yield.

Among the several reactor configurations,^{3–8} membrane reactors showed a promising future and thus attracted increasing interest in the scientific community for OCM because of their advantages in terms of enhanced catalytic activity and selectivity, combination of processes (reaction and separation), simplicity in process design, and safety in operation. This could be also considered as an extension of the oxygen-distributed feed reactor where the number of injection points was infinite. The use of membrane reactors also has advantages in controlling the hot spots in exothermic reactions.^{9,10} Over the past decade OCM was studied mostly in porous and dense ceramic membranes. OCM with porous ceramic was first studied where modified commercial alumina tube was used as the membrane.^{11,12} Later on, Ramachandra and co-workers studied OCM using a modified porous Vycor membrane with Sm₂O₃ as a catalyst.¹³ In addition, two-layer porous membranes, with one layer acting as the support and the other acting as the separating layer, were also reported for the OCM reaction.^{14–16} Though these membranes are highly stable, their low selectivity to oxygen arouses

the development of dense mixed oxygen ionic and electronic conducting membranes which facilitate the use of air as oxygen source and thus reduce the operating cost remarkably.^{17–21} However, due to less oxygen permeation in these types of membrane, OCM has recently been studied in a hollow fiber membrane reactor.²² This type of membrane provides large membrane area per unit volume for oxygen permeation.

Although possessing the relative advantage of being able to improve the catalytic selectivity and operate at a steady state, membrane reactors did not show significant improvement in overall C₂ yield (maximum 22.5%) for the process to be commercially feasible. Only in one study²³ a yield of 27.5% was reported, where La-modified γ -alumina was used as the membrane. No further development of this kind of membrane was found in the open literature. In all these cases, in addition to the difficulties associated with the permeation of oxygen, the lack of development of the more active and selective catalyst, which would provide high reaction rates at low concentrations of oxygen while maintaining desirable selectivity, is recognized as one of the main impediments. Moreover, the design and operation of the membrane reactors were not subjected to systematic and rigorous mathematical optimization methods. Consideration of the systematic optimization method for optimal design of the membrane and reactor would have helped increase their competitiveness further, i.e., achieved better results, by influencing the distribution of oxygen along the reactor bed.

There has been some work on identifying the optimal operating conditions for improved reactor performance. Optimal operation in porous ceramic membranes, reported by Kao and co-workers, can be regarded as more of a parametric study rather than optimization.²⁴ In another work, Amin and co-workers optimized the operating temperature and inlet oxygen concentration simultaneously to maximize the C₂ yield using response surface methodology.²⁵ Nouralishahi and co-workers reported the optimal temperature profile in a fixed-bed plug flow reactor for OCM and summarized the characteristics of various performance-indicating parameters at this optimal temperature profile.²⁶ Yuen and co-workers first reported how to apply the multiobjective optimization in membrane reactor module design to improve beer dialysis.²⁷ Most of these studies dealt with single-objective optimization as only one objective was maximized or minimized at a time. However, most real-world chemical engineering problems require the simultaneous opti-

* To whom correspondence should be addressed. E-mail: aray@eng.uwo.ca.

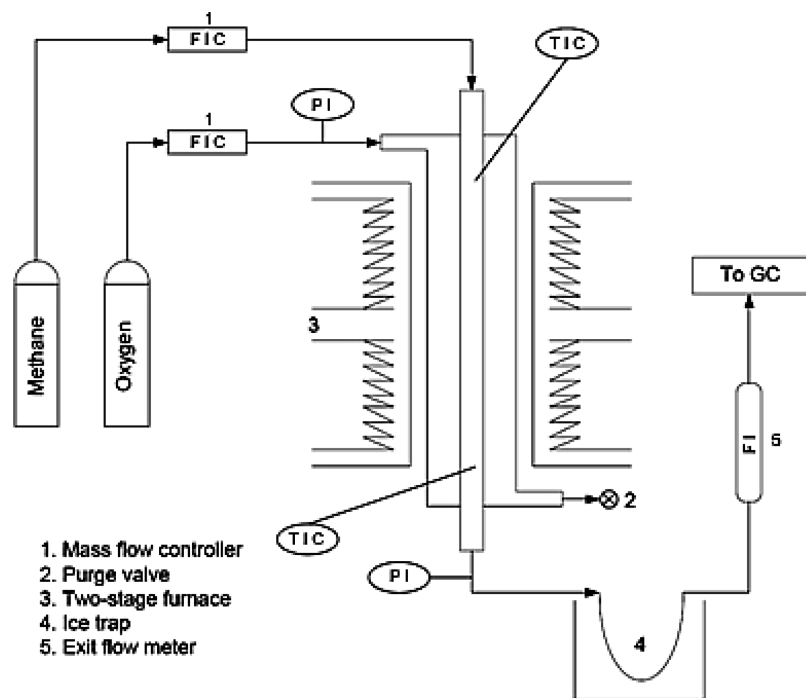


Figure 1. Schematic diagram of the microporous ceramic membrane reactor.

mization of several objectives (multiobjectives) that are non-commensurate. Similarly, the design and operation of membrane reactors require the minimization or maximization of several objectives which are often conflicting. Thus rigorous multiobjective optimization of a membrane reactor is needed.

In this study, systematic investigation of multiobjective optimization of a membrane reactor was first carried out for the OCM reaction. The operating and design parameters of the membrane reactor influence its performance (e.g., selectivity and yield) in noncommensurable ways. Therefore, the results of multiobjective optimization are meant to be more valuable than those from a single-objective optimization. A detailed multiobjective optimization of the foremost membrane reactor for OCM developed by Coronas and co-workers¹² is performed in this study. A mathematical model, similar to the model proposed by Kao and co-workers,²⁴ was developed to describe the process and was subsequently validated by the experimental results.¹² Next, a parametric sensitivity analysis was carried out on the experimentally verified model to systematically investigate the effects of the process parameters on the performance of the membrane reactor. Thereafter the model was interfaced with a state-of-the-art artificial intelligence based robust non-traditional global optimization technique, nondominated sorted genetic algorithm (NSGA),^{28–30} to perform systematic multi-objective optimization study.

2. Process Description

The shell and tube arrangement of the membrane reactor consisted of a fixed bed, packed with catalyst (Li/MgO) which was surrounded by a porous ceramic tube with a length of 30 cm and an internal diameter of 0.66 cm. This tube acted as an oxygen distributor in the reactor. The precise permeation region, 14 cm at the center of the tube, was set by coating both ends with an enamel layer. The shell was made of stainless steel. Details of the reactor configuration, catalyst, and membrane preparation were reported elsewhere.^{12,31} A schematic diagram of the experimental setup of the porous membrane reactor is illustrated in Figure 1.

Methane was fed axially to the tube side, and the flow was controlled accurately by means of a mass flow controller according to Figure 1. Oxygen was fed to the shell side of the membrane reactor. Even though the flow of oxygen was controlled by the applied pressure differential across the membrane, it was continuously monitored using a mass flow meter. Both components were pure and no dilution was employed. Oxygen was allowed to permeate only in the central region of the ceramic tube, and this region was termed as the permeation zone. An external electrical furnace with two independent heating zones was used to heat the reactor.

As seen from Figure 1, the temperature was kept steady inside the catalyst bed using two PID controllers at the two measuring points which were usually located 14 cm apart, at each end of the permeation zone. The exit gases were directed to an online gas chromatograph through an ice trap, where they were analyzed for CH₄, O₂, CO, CO₂, C₂H₆, C₂H₄, and hydrocarbons with three and four carbon atoms. A supplementary flow measurement was used at the reactor exit to measure the flow of the product gas stream after the removal of water.

Controlled flow of species across the membrane is of great importance for methane oxidative coupling, since deep oxidation of methane (or the hydrocarbons) could result in the presence of pure oxygen at high temperature and the catalytic activity of the stainless steel shell. The membrane used in the experiment was modified to prevent the outward diffusion of the reactant and the products, but still the potential existed due to no partial pressure of hydrocarbons on the shell side. Moreover, the effect of homogeneous or gas phase reaction was lowered by keeping the shell side volume very small. Otherwise, the shell side reaction would cause serious degradation in the reactor performance, which was also stated in the experimental investigation by Coronas and co-workers.¹² Thus, the following kinetics model was proposed with the mass balance equations to simulate the reactor characteristics at different operating conditions.

Table 1. Kinetic Parameters for Catalytic Gas Phase Reaction^a

rate constant, ^b K_i	preexponential factor, $k_{0,i}$	activation energy, $E_{a,i}$ (kcal mol ⁻¹)
K_1 (mol cm ⁻³ s ⁻¹ atm ^{-0.5})	2.472×10^7	49.64
K_2 (mol cm ⁻³ s ⁻¹ atm ⁻¹)	1.01×10^1	23.15
K_3 (mol cm ⁻³ s ⁻¹ atm ^{-1.25})	1.013×10^{-3}	4.548
K_4 (mol ⁻¹ cm ³ s atm ^{1.5})	2.093×10^{-4}	-27.94

^a Rate constants were reported by Wang and Lin.¹⁷ ^b $K_i = k_{0,i} \exp(-E_{a,i}/RT)$; $i = 1-4$.

3. Mathematical Modeling

3.1. Reaction Kinetics. The kinetics of oxidative coupling of methane (OCM) is complex enough because of the involvement of many species and the formation of radicals at high temperature. Based on the generally accepted assumptions of the mechanisms of OCM on solid oxide catalyst, a kinetic model proposed by Wang and Lin was used in this study.¹⁷ This kinetic model described the different formation rates for the desired products (ethane and ethylene, C₂) and undesired carbon monoxide and carbon dioxide (CO_x), on Li/MgO packed inside the tube side of the membrane reactor as follows:

$$r_{c,1} = \frac{K_3 p_{O_2}^{1.251}}{4} \left[\left(1 + \frac{8K_2 \frac{C_P}{C_T} p_{CH_4}}{K_3 p_{O_2}^{1.251}} \right)^{0.5} - 1 \right] + 16S_0 K_2 \frac{C_P}{C_T} p_{C_2} \quad (1)$$

$$r_{c,2} = \frac{K_3 p_{O_2}^{1.251}}{16} \left[\left(1 + \frac{8K_2 \frac{C_P}{C_T} p_{CH_4}}{K_3 p_{O_2}^{1.251}} \right)^{0.5} - 1 \right]^2 - 8S_0 K_2 \frac{C_P}{C_T} p_{C_2} \quad (2)$$

$$\frac{C_P}{C_T} = \frac{K_1 p_{O_2}^{0.5}}{K_1 p_{O_2}^{0.5} + K_1 K_2 K_4 + K_2 (p_{CH_4} + 8S_0 p_{C_2})} \quad (3)$$

$$S_0 = \frac{2}{\left(1 + 8Z \frac{K_2 p_{CH_4}}{K_3 p_{O_2}^{1.251}} \right)^{0.5} + 1} \quad (4)$$

$$Z = \frac{K_1 p_{O_2}^{0.5}}{K_1 p_{O_2}^{0.5} + K_1 K_2 K_4 + K_2 p_{CH_4}} \quad (5)$$

The formation rates for CO_x and C₂, defined in eqs 1 and 2, are related to the partial pressures of oxygen, methane, C₂ products and temperature. The values of the rate constants are summarized in Table 1. In the tubular membrane reactor, the concentration gradient of oxygen across the catalyst surface was evident and the maximum occurred near the membrane tube wall because of mass transfer resistance. Following the concept of the simultaneous reaction and diffusion in a porous catalyst cylinder, the reaction rate in the packed bed within the membrane tube was correlated to the reactant concentration near the inner membrane tube wall with effectiveness factor which is defined as follows:

$$\eta = \frac{r_{c,i}^a}{r_{c,i}}, \quad i = 1, 2 \quad (6)$$

here $r_{c,i}^a$ is the actual reaction rate within the tube and $r_{c,i}$ represents the ideal reaction rate, if no diffusion resistance is present, stated above from eqs 1 and 2. The value of $\eta = 0.27$

Table 2. Kinetic Parameters for Noncatalytic Gas Phase Reaction^a

products	preexponential factor, $k_{0,i}$ (mol s ⁻¹ atm ^{-α-β})	activation energy, $E_{a,i}$ (kcal mol ⁻¹)	methane dependence, α_i	oxygen dependence, β_i
C ₂ H ₆	3.95×10^5	51.8	1.04	1.78
C ₂ H ₄	9.75×10^4	52.1	1.16	1.62
CO	3.23×10^{11}	71.6	0.53	3.70
CO ₂	1.02×10^{-2}	29.5	-0.95	1.33

^a These values were reported by Lane and co-workers.³²

was obtained by fitting the experimental data reported by Coronas and co-workers.¹³ However, in the case of optimization studies, η was calculated as a function of the Thiele modulus for cylindrical geometry as follows:

$$\eta = \frac{2}{h^2} \left(\frac{h}{\tanh h} - 1 \right) \quad (7)$$

where h is the Thiele modulus.

For the noncatalytic homogeneous gas phase reaction in the shell side of the reactor, the power-law rate expressions³² in eq 8 were used for each of the major products based on the feed partial pressures of methane and oxygen as shown in Table 2. Like the reaction rates expressed for the catalytic side, the reaction rates in the shell side of the reactor were also expressed as the lumped rates for C₂ and CO_x products as shown in eqs 9 and 10:

$$r_i = (k_{0,i} \exp(-E_{a,i}/RT)) p_{CH_4}^{\alpha_i} p_{O_2}^{\beta_i} \quad (8)$$

$$r_{g,1} = r_{CO} + r_{CO_2} \quad (9)$$

$$r_{g,2} = r_{C_2H_6} + r_{C_2H_4} \quad (10)$$

where r_{CO} , r_{CO_2} , $r_{C_2H_6}$, and $r_{C_2H_4}$ are the homogeneous reaction rates defined in eq 8.

3.2. Permeation through the Porous Membrane. The gas permeation through the commercial alumina microfiltration membrane was governed by Knudsen diffusion, molecular diffusion, and viscous flow. At high temperature and low pressure Knudsen diffusion is the dominant mechanism.¹² The diffusion flux of each species was calculated according to the following equation:

$$J_i = \frac{D_{i,k}}{RT} \left(\frac{p_i^t - p_i^s}{\delta} \right) \quad \text{with } i = CH_4, O_2, C_2H_4, C_2H_6, CO, CO_2, \text{ and } H_2O \quad (11)$$

In eq 11, J_i is the permeation flux, $D_{i,k}$ is the Knudsen coefficient, p_i^t and p_i^s are the partial pressure at the tube and shell side respectively for each species, and δ is the thickness of the membrane. The Knudsen coefficient was calculated by the following correlation.³³

$$D_{i,k} = \frac{2\varepsilon}{3\tau} r \left(\frac{8RT}{\pi M_i} \right)^{0.5} \quad (12)$$

where $\varepsilon = 0.5$ is the porosity, $\tau = 2.95$ is the tortuosity, and $r = 2 \times 10^{-7}$ cm is the pore diameter of the membrane. M_i is the molecular weight of each species. The values of ε , τ , and r reported here were obtained from the literature for the ceramic membrane.³⁴ However, in the experiment, the ceramic membrane used was modified and details of the membrane properties after modification were not reported by Coronas and co-workers.¹² Hence, the permeabilities were found to be about

Table 3. Mathematical Models of the Membrane Reactor for OCM

$$\frac{dF_{CH_4}^t}{dz} = -A^t(r_{c,1}^a + 2r_{c,2}^a) - \pi d^t J_{CH_4} \quad (13)$$

$$\frac{dF_{O_2}^t}{dz} = -A^t(2r_{c,1}^a + 0.5r_{c,2}^a) - \pi d^t J_{O_2} \quad (14)$$

$$\frac{dF_{CO_x}^t}{dz} = A^t r_{c,1}^a - \pi d^t J_{CO_x} \quad (15)$$

$$\frac{dF_{C_2}^t}{dz} = A^t r_{c,2}^a - \pi d^t J_{C_2} \quad (16)$$

$$\frac{dF_{H_2O}^t}{dz} = A^t(2r_{c,1}^a + r_{c,2}^a) - \pi d^t J_{H_2O} \quad (17)$$

$$\frac{dF_{CH_4}^s}{dz} = -\frac{r_{g,1} + 2r_{g,2}}{L} + \pi d^s J_{CH_4} \quad (18)$$

$$\frac{dF_{O_2}^s}{dz} = -\frac{2r_{g,1} + 0.5r_{g,2}}{L} + \pi d^s J_{O_2} \quad (19)$$

$$\frac{dF_{CO_x}^s}{dz} = \frac{r_{g,1}}{L} + \pi d^s J_{CO_x} \quad (20)$$

$$\frac{dF_{C_2}^s}{dz} = \frac{r_{g,2}}{L} + \pi d^s J_{C_2} \quad (21)$$

$$\frac{dF_{H_2O}^s}{dz} = \frac{2r_{g,1} + r_{g,2}}{L} + \pi d^s J_{H_2O} \quad (22)$$

$$z = 0, \quad F_{CH_4}^t = F_{CH_4}^0; \quad F_{O_2}^t = F_{O_2}^0; \quad F_i^s = 0 \text{ and } F_i^t = 0 \quad (23)$$

^a F_i^0 and F_i^t are in mol s⁻¹.

1/23 of the calculated values using eq 12 by fitting the experimental results.¹² A similar value²⁴ was also reported by Kao et al.

3.3. Reactor Model. The model equation for the microporous ceramic membrane reactor (CMR) is based on the assumption of plug flow reactor configuration as axial dispersion was considered negligible. It was also assumed that the temperature inside the reactor was constant and the same for both sides. The pressure drop through the packed bed in the tube side was negligible, and the shell side pressure was constant at steady state condition. Models for the membrane reactor for the OCM reaction are summarized in Table 3.

Though isothermal condition was assumed, the actual reactor operation was neither isothermal nor adiabatic. Significant changes in the temperature of the reaction environment were reported due to the variation of methane feed rate and resultant conversion.¹² This could be due to the proportional increase of the heat released during the reaction by the increased feed flow rates of the reactant. However, at a fixed feed rate the reactor approached near-isothermal condition as the uniform distribution of oxygen throughout the reactor resulted in a uniform temperature throughout the reactor length.¹⁰ Therefore consideration

Table 4. Simulation Parameters

parameter	value
W/F (g min cm ⁻³)	0.01–0.07
W (g)	4.7
$F_{CH_4}^0/F_{O_2}^0$	4
L (cm)	14
d_t (cm)	0.66
P^t (atm)	1
P^s (atm)	1.21–2.6
T (K)	963–1063
η	0.27

of isothermal temperature for the modeling equation is justifiable enough. The isothermal temperature at the highest and lowest feed conditions was reported to be 1063 and 963 K, respectively.²⁴ The isothermal temperatures at intermediate flow rates were determined by linear interpolation between these two limits as the heat of reaction released was proportional to the feed rate. The partial pressure of the oxygen in the shell side was varied from 0 to 6 atm. At a lower value of methane feed rate, the reactor entrance required a corresponding reduction in the amount of oxygen permeated through the membrane. This was achieved by decreasing the pressure on the shell side to values which were reported to be sometimes below 1.5 atm of absolute pressure. The operating pressures at the highest and lowest space times were reported to be 2.6 and 1.21 atm, respectively, by Kao and co-workers.²⁴ Therefore, linear interpolation of the shell side pressure (P^s) was done at the specific feed rate combination with the values stated above. The tube side was operated at pressure (P^t) equal to 1 atm, and the pressure drop along the length of the tube was considered negligible.

All the model equations for both the shell and tube sides were solved in succession using Compaq Visual Fortran 6.6. Ordinary differential equations were solved numerically with Gear's BDF method, using the DIVPAG subroutine of the IMSL library. Parameters used in the simulation are summarized in Table 4.

To validate the model, conversion of methane and selectivity of C₂ products are compared with the experimental data¹² as shown in Figure 2. It could be concluded that the model could provide extremely good predictions of the experimental conversion and selectivity with the variation of space time (W/F) defined as the ratio of catalyst weight to the feed flow rate of methane.

4. Multiobjective Optimization

Optimization problems for CMR can be defined in various ways, including minimization of the fixed costs or operating costs and/or maximization of the production rate or profit. However, the cost and profit depend on demand and prices of raw material and products which are site and time dependent, as well as the downstream processing costs, and therefore might not always provide a meaningful optimization. This study is focused on defining meaningful objective functions so that results can be used independent of location and time. Therefore, conversion of methane (X_{CH_4}), yield (Y_{C_2}), and selectivity (S_{C_2}) of C₂ as well as flow rate of C₂ and CO_x were chosen as the objectives among which X_{CH_4} , Y_{C_2} , and S_{C_2} were defined as follows:

$$X_{CH_4} = \frac{2[\text{mol of } C_2 (C_2H_6 + C_2H_4)] + CO_2/CO}{\text{mol of } CH_4 \text{ fed}} \quad (24)$$

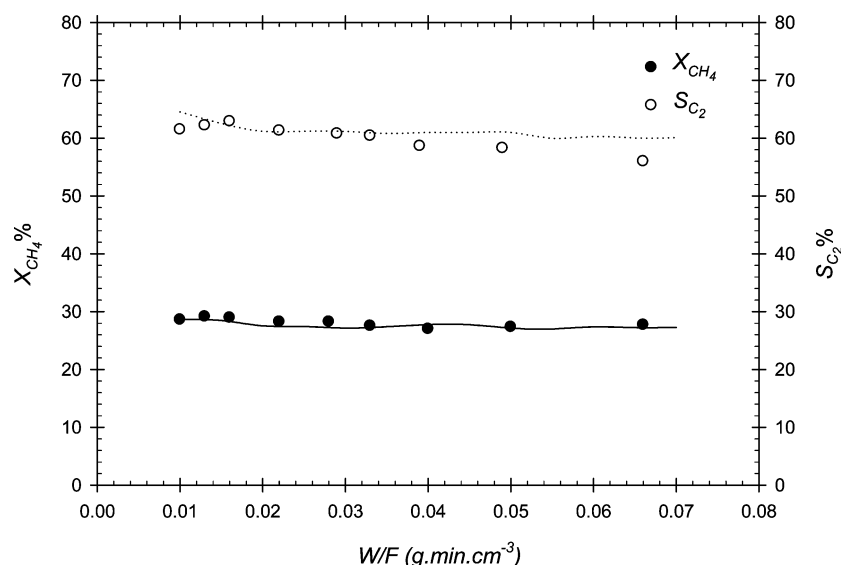


Figure 2. Comparison of model-predicted values of conversion and selectivity with the experimental data reported by Coronas and co-workers.

Table 5. List of Design and Operating Stage Optimization Problems

problem no.	objective function	decision variables	constraints	fixed variables
Operating Stage				
case 1	max Y_{C_2} ; max S_{C_2}	$100 \leq F_T \leq 600 \text{ cm}^3 \text{ min}^{-1}$; $0.0 < F_{CH_4}^0/F_T < 1.0$	$1.0 \leq P^s \leq 6.0 \text{ atm}$; $963 \leq T \leq 1063 \text{ K}$	$L = 14 \text{ cm}$; $d^f = 0.66 \text{ cm}$; D_{rk}
case 2	max F_{C_2} ; min F_{CO_x}			
Design Stage				
case 3	max Y_{C_2} ; max S_{C_2}	$100 \leq F_T \leq 600 \text{ cm}^3 \text{ min}^{-1}$; $0.0 < F_{CH_4}^0/F_T < 1.0$;	$1.0 \leq P^s \leq 6.0 \text{ atm}$; $963 \leq T \leq 1063 \text{ K}$	D_{rk}
case 4	max F_{C_2} ; min F_{CO_x}	$11.0 \leq L \leq 16.0 \text{ cm}$; $0.6 \leq d^f \leq 0.7 \text{ cm}$		

Table 6. Values of the Computational Parameters Used in NSGA-II-aJG

parameters	values
number of generations, N_{gen}	200
number of populations, N_{pop}	50
length of substring for each decision variables, l_{substr}	32
crossover probability, p_c	0.7 ^a
mutation probability, p_m	0.005 ^a
jumping probability, p_{jG}	0.15 ^a
seed for random number generator, S_r	0.287

^a In the design stage problem $p_c = 0.71$, $p_m = 0.002$, and $p_{jG} = 0.11$.

$$S_{C_2} = \frac{2[\text{mol of } C_2 (C_2H_6 + C_2H_4)]}{2[\text{mol of } C_2 (C_2H_6 + C_2H_4)] + \text{mol of } C_1 (CO_2/CO)} \quad (25)$$

$$Y_{C_2} = \frac{2[\text{mol of } C_2 (C_2H_6 + C_2H_4)]}{\text{mol of } CH_4 \text{ fed}} \quad (26)$$

4.1. Sensitivity Analysis. A sensitivity analysis was performed with the CMR model to understand the influence of individual operating and design parameters, which were used as decision variables in the subsequent optimization study. Sensitivity analysis is one of the key tools to formulate any optimization problem appropriately. The effects of total feed flow rate (F_T), feed ratio of methane to oxygen or methane to total feed flow ($F_{CH_4}^0/F_T$), length (L), and diameter (d^f) of the reactor on performance-indicating parameters X_{CH_4} , S_{C_2} , yield (Y_{C_2}), production rate of C_2 product (F_{C_2}), and production rate of CO_x product (F_{CO_x}) were studied. The values of each of these variables were varied within $\pm 10\%$ of the reference value one at a time keeping the others constant at the reference value. The complete result of the analysis is depicted in Figure 3. The performance-indicating parameters are plotted using the

same scale throughout the figure so that the degree of the influence of each decision variable is easily discernible. The relative changes in the performance-indicating parameters from the reference values are also presented in Figure 3.

The effect of the total feed flow on CMR performance illustrates that an increase in the flow rate results in an insignificant effect on the selectivity and a slight increase in the conversion. The production rates of both C_2 and CO_2 increased steadily with the flow rate. However, the formation rate of C_2 became steeper while the CO_x production maintained the same rate of formation beyond the reference point of operation. This was due to the decrease in the residence time which in turn prevented the deep oxidation of formed C_2 product. Thereby, after the reference point, the slope of CO_x formation rate of was unchanged as most of the CO_x that was produced was from the oxidation of CH_4 only.

The decrease in the feed ratio ($F_{CH_4}^0/F_T$) or the decrease in $F_{CH_4}^0$ with an increase in oxygen feed rate ($F_{O_2}^0$) had a greater influence than the other decision variables on the performance of the CMR. As the ratio was decreased, X_{CH_4} was increased accompanied by the decrease in S_{C_2} . Y_{C_2} and F_{C_2} increased up to a certain feed ratio and then started to decrease because of the greater availability of the gas phase oxygen which favored the deep oxidation of CH_4 and formed C_2 products. With the increasing $F_{O_2}^0$, the variation of F_{CO_x} was monotonic.

Both variables L and d^f had a significant effect on the performance parameters X_{CH_4} , Y_{C_2} , F_{C_2} , and F_{CO_x} , though S_{C_2} was invariant to the change. From Figure 3 it was evident that the gas phase concentration of oxygen was less at the end of the reactor. This end condition favored the formation of C_2 products and prevented the deep oxidation of both the reactants and C_2 products. Hence, as the length of the reactor was increased an increase in X_{CH_4} and Y_{C_2} was the consequence and

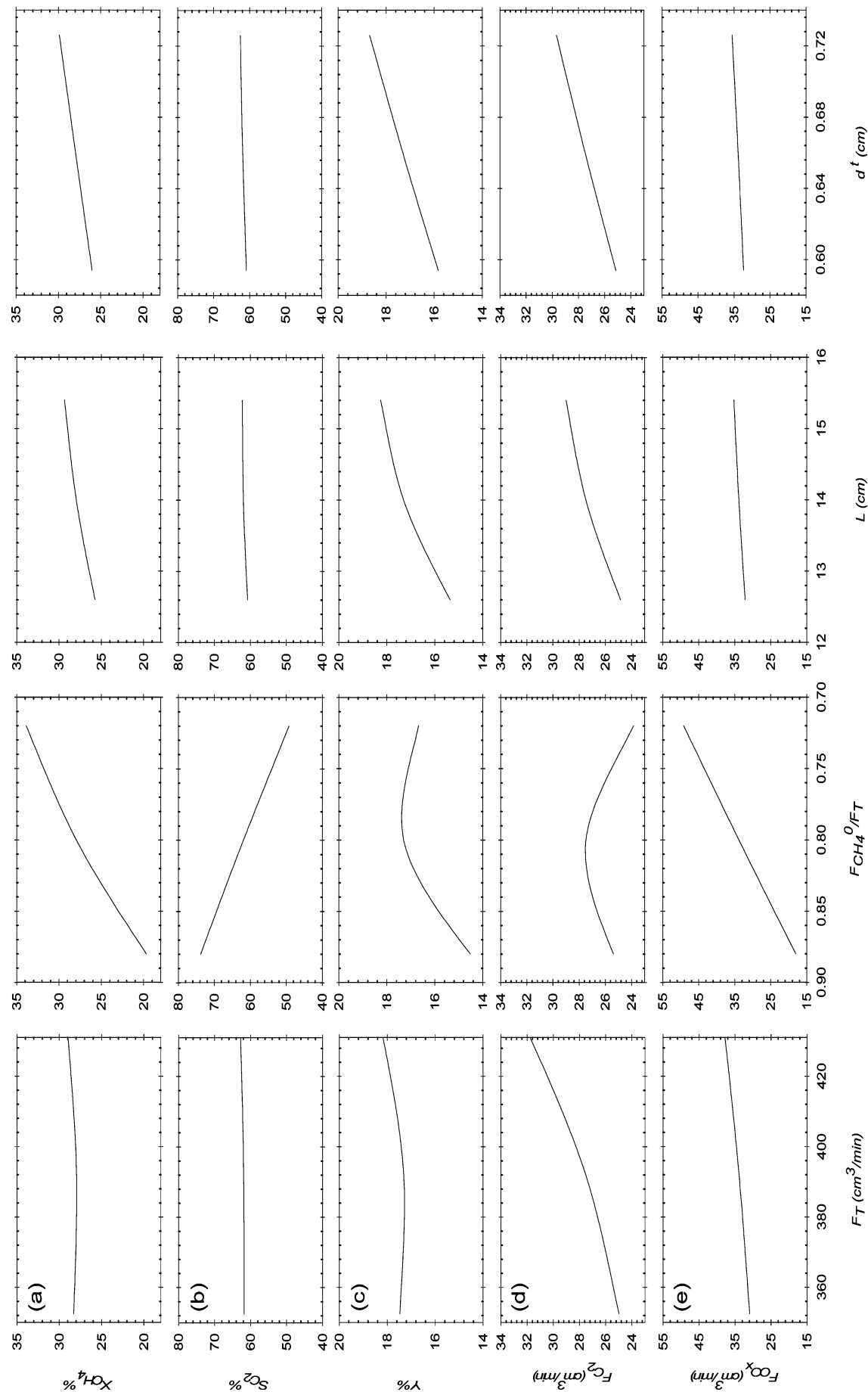


Figure 3. Effect of decision variables on performance of ceramic membrane reactor.

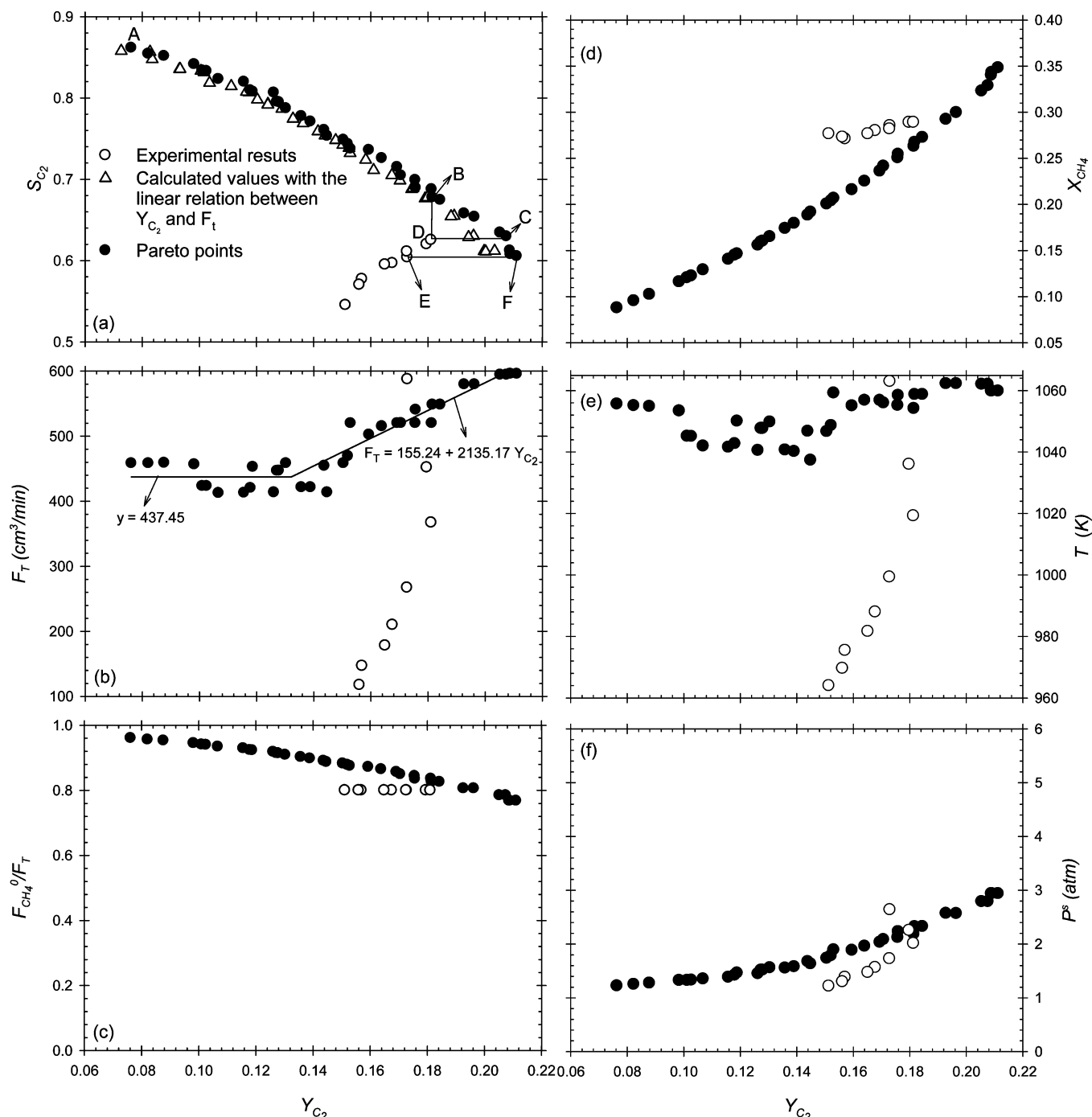


Figure 4. Pareto optimal solutions of case 1.

a more precipitous change in the C_2 formation than in the formation of CO_2 products was observed. Apart from this, as the diameter increased, more oxygen was allowed to permeate to the tube side and thus accelerated the rates of reaction. However, this also accompanied by a resulting decrease in the concentration of oxygen at the center of the tube due to more diffusional resistance for oxygen molecule. Therefore, deep oxidation mostly occurred adjacent to the tube wall, whereas it was less away from the wall and at the center of the tube. Thus the formation of C_2 products was more facilitated than in the tube with small diameter.

From the discussion it is obvious that all the results that were obtained from sensitivity analysis can be explained qualitatively and all the trends followed anticipated behavior. This established

the robustness of the model, and thus using this model for optimization study was rational enough.

4.2. Multiobjective Optimization Using NSGA-II-aJG. It has been proven from the sensitivity analysis that decision variables have conflicting influences on the performance parameters, and it is not possible to maximize the conversion, yield, selectivity, and formation rate of C_2 products, and/or to minimize the formation rate of CO_x products simultaneously. One must perform a systematic multiobjective optimization (MOO) study to determine the optimal operating conditions and design configurations of the CMR unit.

Among the several available methods for solving the MOO problems, the nondominated sorting genetic algorithm (NSGA) has been widely used. NSGA differs from the simple GA only

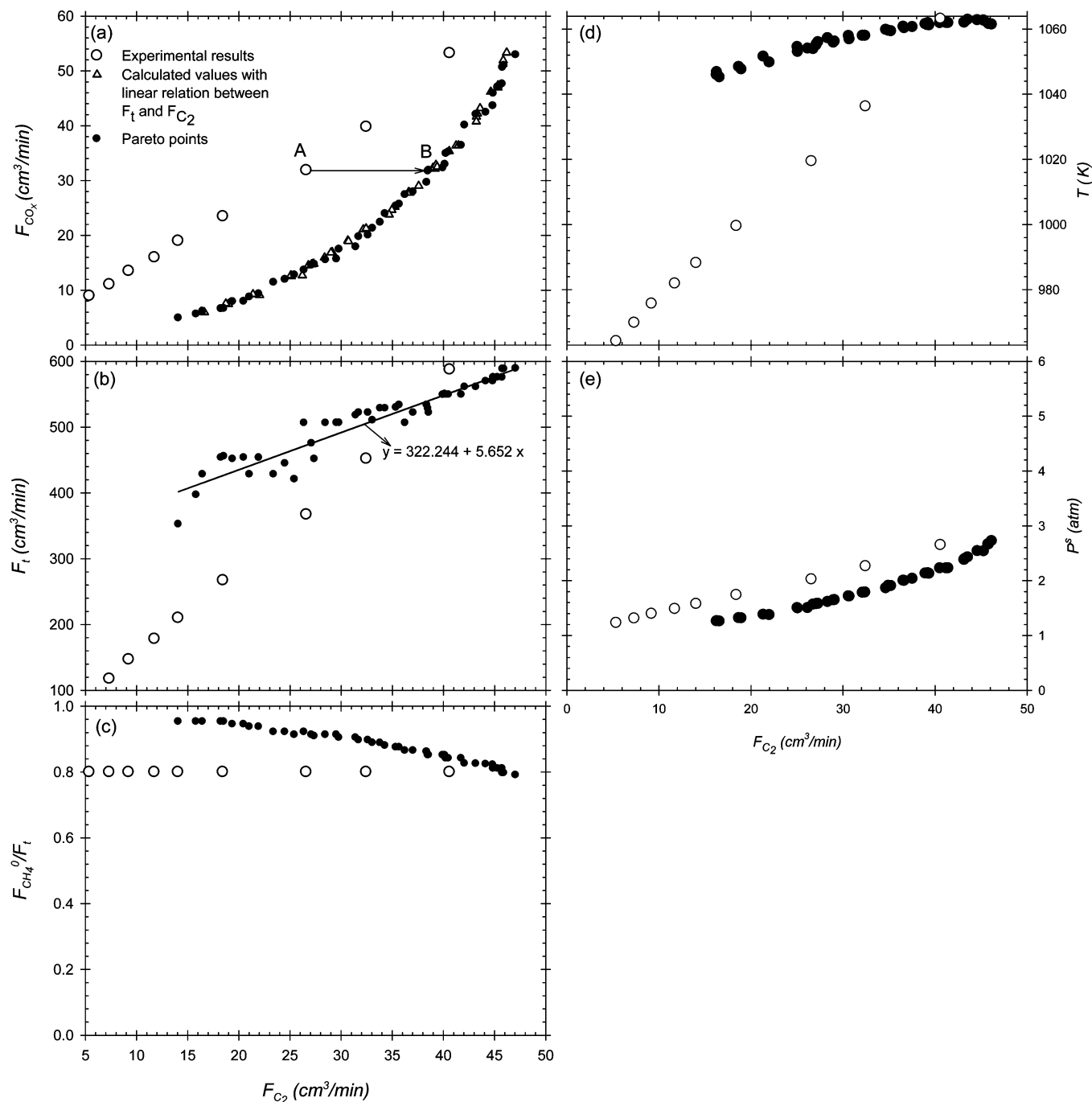


Figure 5. Pareto optimal solution of case 2.

in the way the selection operator works.³⁵ NSGA uses a ranking selection method to emphasize the good chromosomes and a niche method to create diversity in the population without losing a stable subpopulation of good chromosomes. NSGA-II³⁶ is a further improvement of NSGA; it is an elitist NSGA using an elite-preservation strategy as well as an explicit diversity-preserving mechanism. By applying elitism better convergence near the true Pareto optimal front and better spread of Pareto optimal solutions was obtained, but resulted in decreased genetic diversity. Kasat and Gupta³⁷ introduced the concept of jumping genes in NSGA-II, and the adaptation is referred to as NSGA-II-JG. They applied NSGA-II-JG to optimize the same fluidized-bed catalytic cracking unit and showed that the adaptation was able to maintain genetic diversity and at the same time also reduce computation time. In this work, all the MOO problems were solved using NSGA-II-aJG,³⁸ an improved version of

NSGA-II. Table 5 summarizes the formulations of the MOO problems studied in this work. Computational parameters used for NSGA-II-JG in this study are given in Table 6.

4.3. Case Study of Multiobjective Optimization. MOO problems for the CMR unit were studied at both the operating and design stages in this work. The objective functions and corresponding decision variables are plotted and compared with the corresponding experimental values. Later on, results obtained at the operating stage and design stage are also compared.

4.3.1. Operating Stage Optimization. Case 1: Maximization of Yield (Y_{C_2}) and Selectivity (S_{C_2}). Maximizations of yield and selectivity were selected as the two objectives of case 1. The formulation of this optimization problem is summarized in Table 5. Figure 4a illustrates the Pareto optimal set obtained for case 1. A contradictory behavior is observed between the

two objectives; i.e., moving from the left to the right (for example, from point A to C) the Y_{C_2} increases at the cost of reduced S_{C_2} . Hence, each point on the Pareto set is equally good. The maximum possible S_{C_2} is 85.15%, while the maximum possible yield exceeds the experimental results by 16.5% and is equal to 21.11%. Each point on the Pareto optimal front corresponds to a set of decision variables, which are plotted in Figure 4b,c against Y_{C_2} . The maximum and minimum values of the y-axis in Figure 4b,c represent the upper and lower bounds of the respective decision variables. Among the decision variables the feed flow ratio ($F_{CH_4}^0/F_T$) is the most sensitive one with respect to Y_{C_2} and S_{C_2} , and the Pareto is mainly formed because of the conflicting behavior of $F_{CH_4}^0/F_T$ on the two objective functions. Figure 4c shows that, with the decrease in $F_{CH_4}^0/F_T$, Y_{C_2} increases while S_{C_2} decreases, which is expected from the sensitivity analysis results discussed earlier. With the decrease in $F_{CH_4}^0/F_T$, more oxygen is allowed to permeate the tube side and as a result conversion (X_{CH_4}) increases while selectivity decreases. X_{CH_4} against Y_{C_2} is plotted in Figure 4d for each of the chromosomes of the Pareto solutions obtained above. The constraints corresponding to the optimal solution are also plotted in Figure 4e,f. The shell side pressure varies inversely with $F_{CH_4}^0/F_T$. As the ratio decreases, the shell side pressure is increased for permeation of more oxygen to the tube side. The optimal values of the total feed rate (F_T) are slightly scattered initially and later rise to the maximum. This is due to the less sensitive characteristics of this decision variable to the objectives. From sensitivity analysis it was obvious that S_{C_2} was not at all sensitive to F_T whereas slight sensitivity was observed in case of Y_{C_2} . This insensitivity was also substantiated by choosing a constant value of F_T up to a Y_{C_2} value of 13.21% and later on using a linear relationship between Y_{C_2} and F_T . The lines are shown in Figure 4b with the equations. The corresponding values of S_{C_2} and Y were calculated with the same values of $F_{CH_4}^0/F_T$ and are also plotted with triangle symbols (Δ) in Figure 4a. It is seen that these results coincide with the Pareto front. Therefore, from the operational viewpoint these equations of lines should be more suitable to use than the scatter values resulting from the analysis.

Figure 4a also shows the current experimental operating points (open circle symbols). Point D is always better than point E in terms of both Y_{C_2} and S_{C_2} . However, all the points on the Pareto set are much better than the current operating points. Y_{C_2} was increased by $\sim 15\%$ for a fixed S_{C_2} (point D to point C) or S_{C_2} could be improved by $\sim 8\%$ without decreasing the current Y_{C_2} (point B over point D). Selection of a point from the entire Pareto sets for the efficient operation depends on other factors such as cost of the feed, downstream processing, operating costs, etc., which are site and time specific. Of the two objectives which one is more important depends on these factors.

With a small sacrifice in the current maximum operating value of S_{C_2} , one can achieve a much higher Y_{C_2} (21.11%, point F) with an increase in the pumping cost. However, at the highest operating flow rate (point E), one can increase Y_{C_2} by 16% (point F) just by changing the feed ratio. Though it would be obtained by a slight increase in the pumping cost of oxygen, the temperature in this case is lower than the current operating condition shown in Figure 4e. However, Figure 4 provides a wide range of competing options for the improvement over the current operation.

Case 2: Maximize C_2 Flow (F_{C_2}) and Minimize CO and CO_2 Flow (F_{CO_x}). Maximization of F_{C_2} was considered as an objective function in this problem as C_2 is the most valuable product for enhancing the profit, while for environmental

consideration the deep oxidation of methane was minimized, which reduces the formation and emission of greenhouse gases, F_{CO_x} . Figure 5a portrays the Pareto optimal set obtained for the simultaneous maximization of F_{C_2} and minimization of F_{CO_x} . Every point on the Pareto denotes the maximum C_2 production possible and at the same time the minimum formation of CO_x by varying the operating conditions, F_T and $F_{CH_4}^0/F_T$. Moreover, it is apparent that a slight increase in F_{CO_x} facilitates to achieve a greater value of F_{C_2} . The experimental results (open circle symbols) are also plotted with the Pareto front, which reveals the improvement possible beyond the current operating conditions. The C_2 production could be increased by 46% from the current operating condition by producing the same amount of CO_x (from point A to point B). At this point (A) the operational yield was maximum (point D in Figure 4a).

The decision variables and values of the constraints corresponding to the Pareto set shown in Figure 5a are plotted against F_{C_2} in Figure 5b–e, respectively. Though the objective space converged to a Pareto with a good spread, the variable space of F_T is scattered and less than in case 1.

This is due to greater sensitivity of F_T to the objectives compared to case 1. From sensitivity analysis it was expected that F_T should hit the upper bound (maximum value allowed) of the flow rate as C_2 production increases with increasing F_T . However, an increment in F_T was also accompanied by an increase in F_{CO_x} . Hence, due to the conflicting nature of the objectives a gradual increase to the highest bound was observed in this case. Again, as in case 1, a linear relationship between F_T and F_{C_2} was established and corresponding values of the linear line are also shown as triangle symbols (Δ) in Figure 5a. Overlapping of the results with the Pareto trend justified the less insensitive behavior of F_T compared to $F_{CH_4}^0/F_T$. In this case, the Pareto was also formed because of the conflicting behavior of the $F_{CH_4}^0/F_T$ on the two objective functions. From the sensitivity analysis it was apparent that C_2 formation rates attained a maximum at ~ 0.8 for $F_{CH_4}^0/F_T$. This again transpired in Figure 5c, where the $F_{CH_4}^0/F_T$ value never drops below 0.79.

4.3.2. Design Stage Optimization. The extent of flexibility offered at the design stage optimization to improve the system performance exceeds the constraints present at optimizing the performance of an existing module. At the design stage, several design parameters in addition to the operating parameters become available for optimization. Several design parameters could be incorporated for analysis, i.e., thickness (δ), pore radius (r), porosity to tortuosity ratio (ε/τ) of membrane, internal tube diameter (d^i), length (L) of the reactor, etc. with the existing operating variables. Due to lack of information about the membrane properties, only two decision variables (L and d^i) were considered in addition to the operating variables because of their direct relation to the fixed cost. All the objectives considered at this stage are greatly influenced by these variables.

The influence of these variables individually on the objectives considered were discussed in the sensitivity analysis section (section 4.1). The influences of these design parameters in combinations with the system performance are studied next. Table 5 presents the details of all the problems solved at the design stage.

Case 3: Maximization of Yield (Y_{C_2}) and Selectivity (S_{C_2}). The objectives studied in this case are analogous to case 1 except for the addition of two more decision variables, length (L) and diameter (d^i) of the tube. The Pareto obtained from simultaneous maximization of Y_{C_2} and S_{C_2} is shown in Figure 6a along with the experimental report values. The corresponding

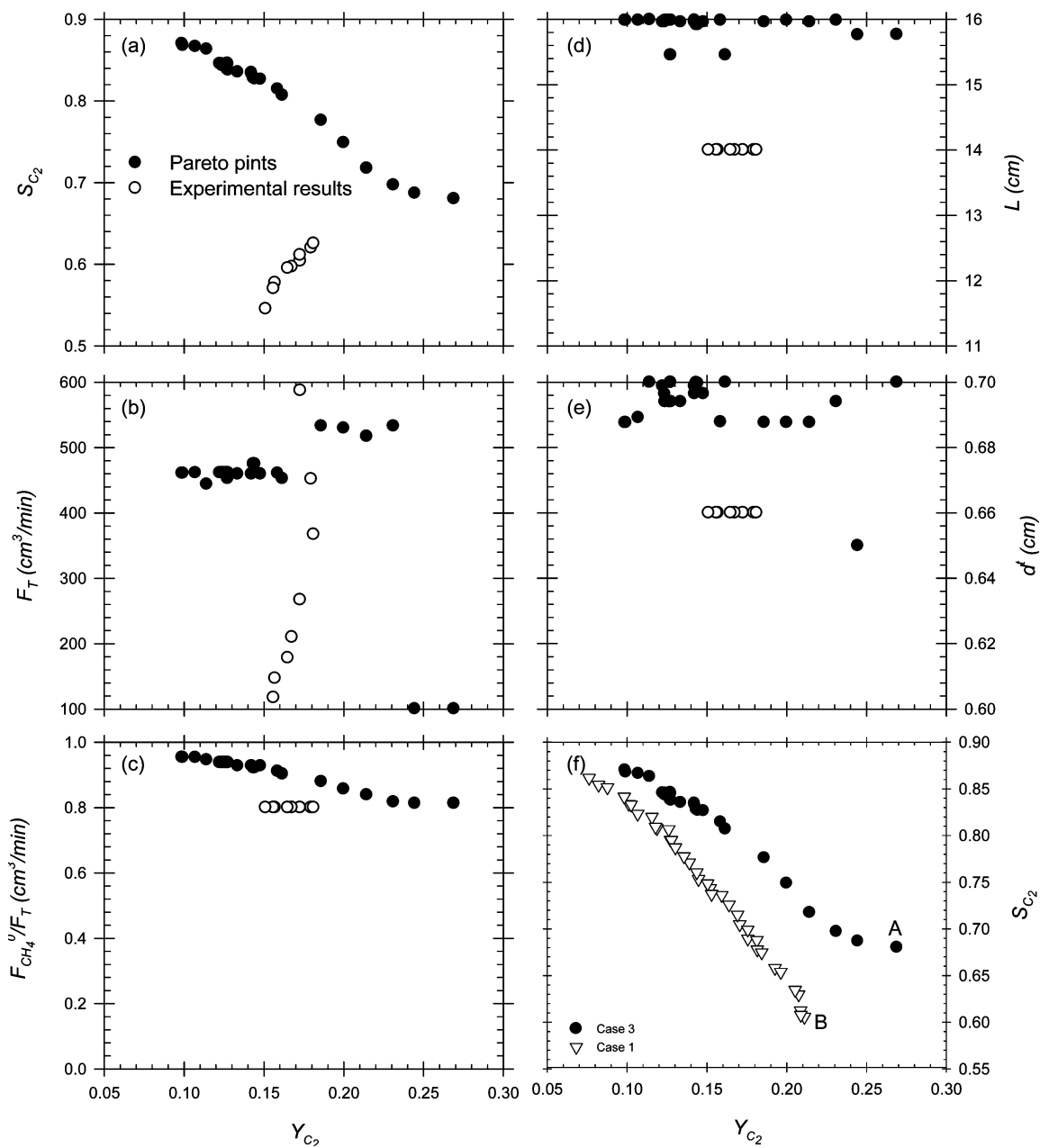


Figure 6. Pareto optimal solutions of case 3.

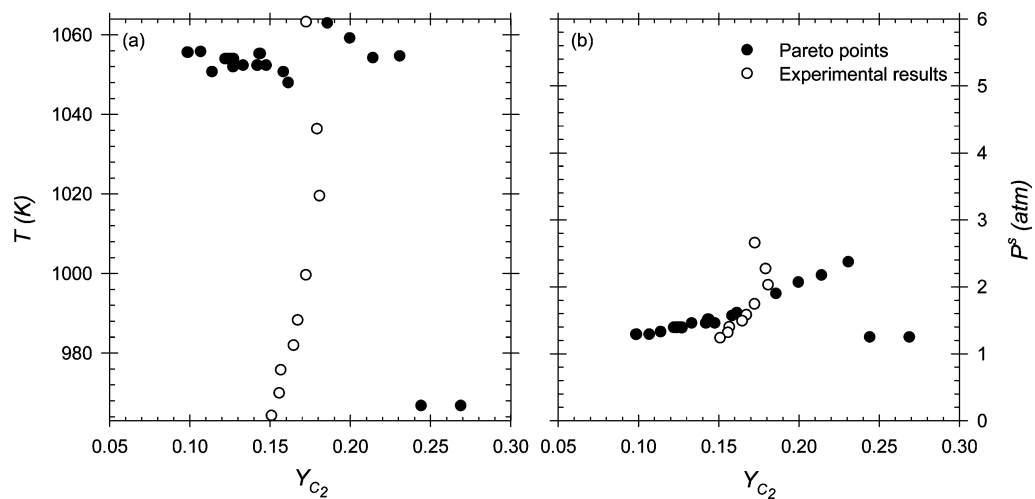


Figure 7. Values of constraints in case 3.

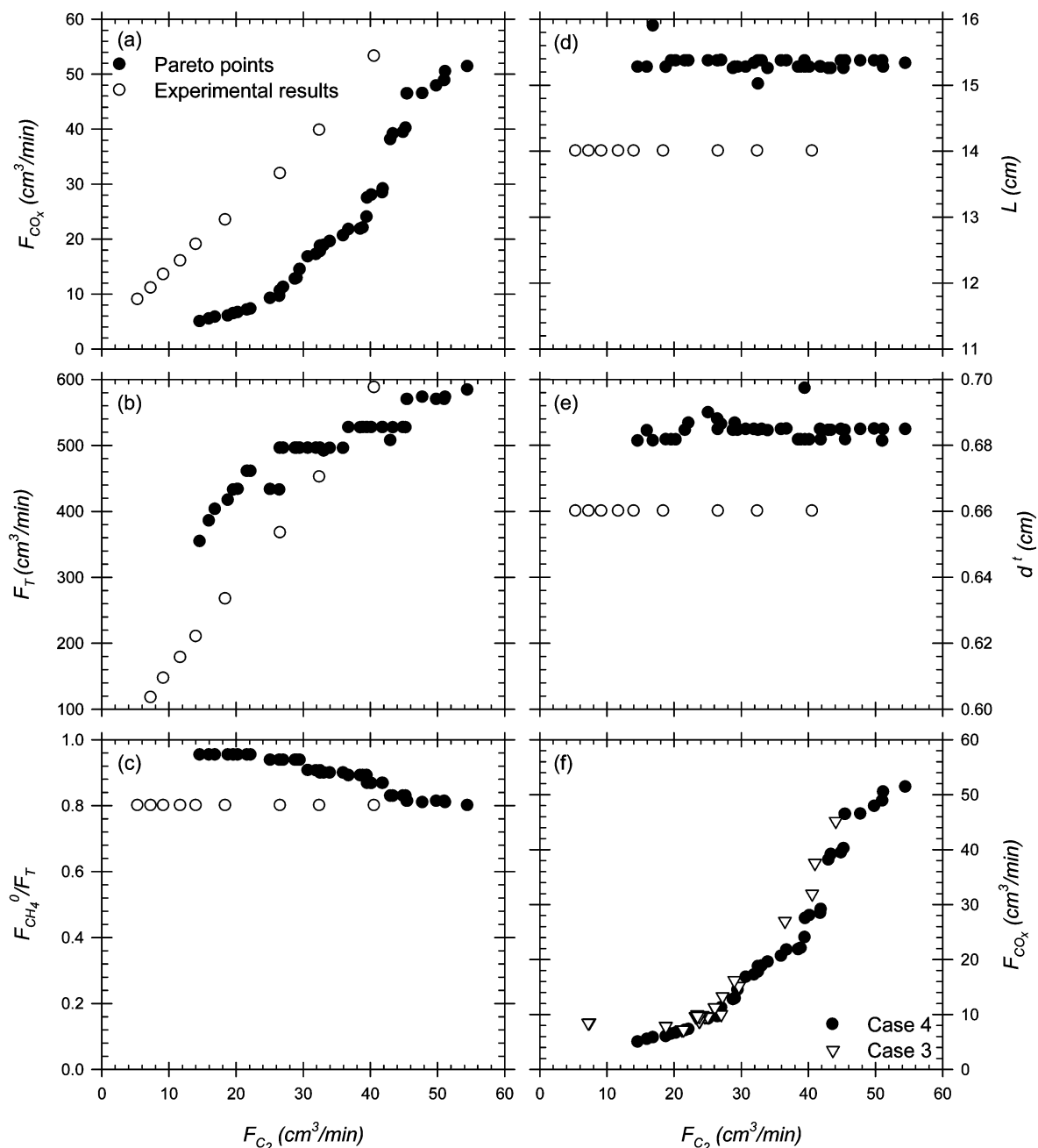


Figure 8. Pareto optimal solutions of case 4.

decision variables are also plotted against Y_{C_2} in Figure 6b–e. The constraints are plotted in Figure 7. Comparison of the two objectives with case 1 is also given in Figure 6f.

The complementary nature of the Pareto followed the same trend as in case 1; i.e., an increase in Y_{C_2} resulted at the cost of reduced S_{C_2} . The maximum yield (27%) surpassed the value obtained in case 1 by 27.4%, whereas an 48.59% increase resulted over the experimental value. Moreover, the value of S_{C_2} at the maximum yield (point A in Figure 6f) in case 3 is also high enough, 13% higher, compared to case 1 (point B in Figure 6f). This is due to the addition of two new design variables in addition to the operating variables, and their concerted influence on the objective functions resulted in these superior optimal results. A higher value of yield around 30% was reported by Kao and Lin in their parametric study.²⁴ In this study the value was a little less due to the incorporation of an effectiveness factor to account for the experimental limitations.

From sensitivity analysis it was expected that the length and tube diameter would hit the upper bound. Figure 6d,e shows this as expected, although there exist slight scattered results around the upper bound. The $F_{CH_4}^0/F_T$ value decreases with increasing yield and is never less than 0.8. All the optimal solutions chose an almost constant value of F_T , i.e., ~ 460 cm³ min⁻¹ up to a yield value of 16.16%, and a higher value, ~ 530 cm³ min⁻¹, after that, except for the last two chromosomes on the right-hand side of Figure 6a. Rather than reaching the upper bound as in cases 1 and 2, F_T hit the lowest bound. This could be explicated by the corresponding decision variables and constraint values of the two optimal solutions in Figures 6b–d and 7. Increasing length facilitates methane to react more near the end of the reactor with the gas phase oxygen, thus increasing the conversion as well as the yield. However, high gas phase concentration of oxygen favors deep oxidation of methane and formed C_2 products, which in turn reduces the selectivity, and

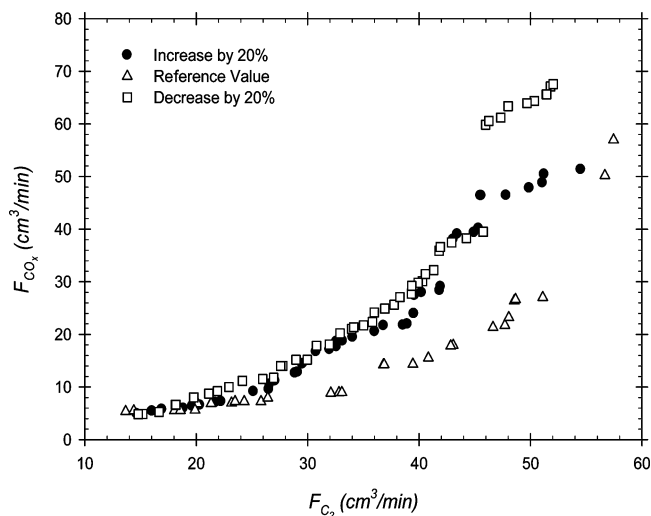


Figure 9. Effect of permeation factor on the Pareto sets of case 4.

thus the yield. This could be attained at a lower value of $F_{CH_4}^0/F_T$ accompanied by a high value of F_T , and thus the increase in differential pressure across the membrane. Besides, a high value of F_T also increases the reaction temperature, which is favorable for both coupling and oxidation reactions. This is why a trade-off between F_T and L resulted in the lowest value of F_T by keeping the L high enough to maximize Y_{C_2} and S_{C_2} at the same time. A high value of L facilitates increased conversion of methane, whereas a low value of F_T prevents deep oxidation of the formed C_2 by keeping the T and P^s low enough. This is also evident from Figure 7.

Case 4: Maximize C_2 Flow (F_{C_2}) and Minimize CO and CO_2 Flow (F_{CO_x}). The results of the simultaneous maximization of F_{C_2} and minimization of F_{CO_x} at the design stage are presented in Figure 8 along with the experimental values. A comparison of the Pareto obtained in this case is also shown in Figure 8f with the calculated values of F_{C_2} and F_{CO_x} in case 3. A slight improvement in the results was obtained due to the trade-off among the decision variables F_T , L , and d^t . The total flow rate in this case is higher than in case 3. Rather than hitting the upper bound, both decision variables L and d^t reached an intermediate optimal value due to the conflicting nature of the objectives.

This case study was also performed with three different values of permeation flux, and the results are illustrated in Figure 9. It is evident that the optimal results are greatly influenced by the changes in permeation flux. With the decrease of permeation flux from the reference value by 20%, which signifies the reduction in permeation of oxygen, the rate of CO_x production increased slightly whereas an increment by 20% greatly increased the production of C_2 with the same formation rate of CO_x . The desired conversion of CH_4 in this case was achieved by increasing the permeation flux which actually enhanced the concentration of oxygen at the end of the reactor and thus facilitated further conversion of CH_4 , whereas in other cases conversion was very low due to lack of oxygen. Therefore, interpretation of the change in permeation flux in terms of membrane physical properties at the design or fabrication stage could aid in obtaining a better permeation pattern of oxygen throughout the reactor.

5. Conclusions

The model developed in this study to simulate the performance of the CMR unit exhibited good conformance with the

experimental results reported by Coronas and co-workers. The model is then used to carry out multiobjective optimization of the CMR unit for OCM in the presence of a few constraints. Several two-objective optimization problems were performed on this model at operating and design stages using a GA based optimizer, NSGA-II-aJG. Formulation of all the problems for optimization was based on sensitivity analysis of the decision variables on the performance parameters of the CMR unit. Two operating variables were chosen for the operating stage optimization, whereas two additional design parameters were incorporated at the design stage. Both at the operating stage and at the design stage, simultaneous maximization of the two most important objectives of the CMR unit, yield and selectivity, were carried out. The results portrayed a substantial increase in C_2 yield, 16.5% at the operating stage and 48.5% at the design stage, from the experimental results. Based on the economic and environmental considerations another multiobjective optimization problem was studied, where maximization of C_2 flow was simultaneously analyzed with minimization of emission of greenhouse gases (CO and CO_2). Slight improvements in the results were discernible compared to the first case. However, incorporation of the influences of membrane properties at the design stage portrayed improved results and thus signifies the possibility of better distribution of oxygen across the reactor. All the results obtained in this study were kept within a feasible search space by including realistic constraints. It was possible to explicate qualitatively the trends of all optimal values of the objectives and the decision variables. Therefore, the reliability of the results was substantiated.

In conclusion, although the desired yield (30% or more) for the OCM reaction in the membrane reactor was not possible to reach for commercial viability, this study showed how application of systematic multiobjective optimization could improve the results of the present operating conditions. Therefore, consideration of the optimization tool at the earlier stages of membrane fabrication, reactor design, and configuration could facilitate the desired level of yield. This study, however, extended the flexibility for a designer to choose the best optimal solutions, and also helped in understanding the performance of the reactors and the trade-off between conflicting objectives and decision variables.

Nomenclature

- A = area (cm^2)
- C = concentration ($mol\ cm^{-3}$)
- C_P = electron-hole concentration
- C_T = electron-hole concentration
- D_k = Knudsen coefficient ($cm^2\ s^{-1}$)
- E_a = activation energy ($kcal\ mol^{-1}$)
- F = flow rate ($cm^3\ min^{-1}$)
- h = Thiele modulus
- J = permeation flux ($mol\ cm^{-2}\ s^{-1}$)
- k = preexponential factor
- K = rate constant
- L = length of the membrane reactor (cm)
- M = molecular weight ($g\ mol^{-1}$)
- p = partial pressure (atm)
- P = total pressure (atm)
- $r_{c,1}$ = catalytic reaction rate for CO_x ($mol\ cm^{-3}\ s^{-1}$)
- $r_{c,2}$ = catalytic reaction rate for C_2 ($mol\ cm^{-3}\ s^{-1}$)
- $r_{g,1}$ = gas phase reaction rate for CO_x ($mol\ s^{-1}$)
- $r_{g,2}$ = gas phase reaction rate for C_2 ($mol\ s^{-1}$)
- R = gas constant ($1.987\ cal\ mol^{-1}\ K^{-1}$)
- S = selectivity

S_0 = fraction of radicals that undergo deep oxidation
 T = temperature (K)
 W = catalyst weight (g)
 X = conversion
 Y = yield
 z = length (cm)
 Z = dimensionless number

Greek Symbols

α = order of reaction
 β = order of reaction
 δ = membrane thickness (cm)
 ε = membrane porosity
 η = effectiveness factor
 τ = tortuosity

Superscripts

0 = feed condition
 a = actual
 s = shell side
 t = tube side

Subscripts

$C_2 = C_2H_6$ and C_2H_4
 $CO_x = CO$ and CO_2
 e = experimental
 m = model

Literature Cited

- (1) Amenomiya, Y.; Birss, V. I.; Golezdzinowski, M. Conversion of Methane by Oxidative Coupling. *Catal. Rev.—Sci. Eng.* **1990**, 32, 227.
- (2) Labinger, J. A. Oxidative Coupling of Methane an Inherent Limit to Selectivity. *Catal. Lett.* **1988**, 1, 137.
- (3) Tonkovich, A. L. Y.; Robert, W. C.; Rutherford, A. Enhanced C_2 Yields from Methane Oxidative Coupling by Means of a Separative Chemical Reactor. *Science* **1993**, 2662, 221.
- (4) Edwards, J. H.; Tyler, R. J. The Oxidative Coupling of Methane in a Fluidized Bed Reactor. *Catal. Today* **1989**, 4, 345.
- (5) Tonkovich, A. L. Y.; Carr, R. W. A Simulated Countercurrent Moving-Bed Chromatographic Reactor for the Oxidative Coupling of Methane: Experimental Results. *Chem. Eng. Sci.* **1994**, 49, 4647.
- (6) Pekediz, A.; de Lasa, H. I. Methane Oxidative Coupling in a Novel Riser Simulator Reactor. *Chem. Eng. Sci.* **1994**, 49, 4759.
- (7) Choudhary, V. R.; Chaudhary, A. M.; Rajput, A. M.; Rane, V. H. Beneficial Effect of Oxygen Distribution on Methane Conversion and C_2 Selectivity on Oxidative Coupling of Methane to C_2 Hydrocarbons Over Lanthanum-Promoted Magnesium Oxide. *J. Chem. Soc., Chem. Commun.* **1989**, 20, 1526.
- (8) Jiang, Y.; Yentekatis, I. V.; Vayenas, C. G. Methane to Ethylene with 85% yield in a Gas Recycle Electrocatalytic Reactor-Separator. *Science* **1994**, 264, 1563.
- (9) Tsai, C.-Y.; Ma, Y. H.; Moser, W. R.; Dixon, A. G. Modeling and Simulation of a Nonisothermal Catalytic Membrane Reactor. *Chem. Eng. Commun.* **1995**, 134, 107.
- (10) Coronas, J.; Gonzalo, A.; Lafarga, D.; Menendez, M. Effect of the Membrane Activity on the Performance of a Catalytic Membrane Reactor. *AIChE J.* **1997**, 43, 3095.
- (11) Coronas, J.; Santamaria, J.; Menendez, M. Methane Oxidative Coupling Using Porous Ceramic Membrane Reactors—II. Reaction Studies. *Chem. Eng. Sci.* **1994**, 49, 2015.
- (12) Coronas, J.; Menendez, M.; Santamaria, J. Development of Ceramic Membrane Reactors with a Non-Uniform Permeation Pattern, Application to Methane Oxidative Coupling. *Chem. Eng. Sci.* **1994**, 49, 4749.
- (13) Ramachandra, A. M.; Lu, Y.; Ma, Y. H.; Moser, W. R.; Dixon, A. G. Oxidative Coupling of Methane in Porous Vycor Membrane Reactors. *J. Membr. Sci.* **1996**, 116, 253.
- (14) Lu, Y.; Dixon, A. G.; Moser, W. R.; Ma, Y. H. Analysis and optimization of cross-flow reactors for oxidative coupling of methane. *Ind. Eng. Chem. Res.* **1997**, 36, 559.
- (15) Chanaud, P.; Julbe, A.; Larbot, A.; Guizard, C.; Cot, L.; Borges, H.; Giroir, F.; Mirodatos, C. Catalytic Membrane Reactors for Oxidative Coupling of Methane, Part I: Preparation and Characterization of LaOCl Membranes. *Catal. Today* **1995**, 25, 225.
- (16) Borges, H.; Giroir-Fendler, A.; Mirodatos, C.; Chanaud, P.; Julbe, A. Catalytic Membrane Reactors for Oxidative Coupling of Methane, Part II: Catalytic Properties of LaOCl Membranes. *Catal. Today* **1995**, 25, 377.
- (17) Wang, W.; Lin, Y. S. Analysis of Oxidative Coupling of Methane in Dense Oxide Membrane Reactors. *J. Membr. Sci.* **1995**, 103, 219.
- (18) Zeng, Y.; Lin, Y. S. Catalytic Properties of Yttria Doped Bismuth Oxide Ceramics for Oxidative Coupling of Methane. *Appl. Catal., A* **1997**, 159, 101.
- (19) ten Elshof, J. E.; Bouwmeester, H. J. M.; Verweij, H. Oxidative Coupling of Methane in a Mixed-Conducting Perovskite Membrane Reactor. *Appl. Catal., A* **1995**, 130, 195.
- (20) Lu, Y.; Dixon, A. G.; Mose, W. R.; Ma, Y. H.; Balachandran, U. Oxygen-Permeable Dense Membrane Reactor for the Oxidative Coupling of Methane. *J. Membr. Sci.* **2000**, 170, 27.
- (21) Akin, F. T.; Lin, Y. S. Oxygen Permeation through Oxygen Ionic or Mixed-Conducting Ceramic Membranes with Chemical Reactions. *J. Membr. Sci.* **2004**, 231, 133.
- (22) Tan, X.; Li, K. Oxidative coupling of methane in a perovskite hollow fiber membrane reactor. *Ind. Eng. Chem. Res.* **2006**, 45, 142.
- (23) Lu, Y.; Dixon, A. G.; Moser, W. R.; Ma, Y. H. Oxidative Coupling of Methane in a Modified Y-alumina Membrane Reactor. *Chem. Eng. Sci.* **2000**, 55, 4901.
- (24) Kao, Y. K.; Lei, L.; Lin, Y. S. Optimal Operation of Oxidative Coupling of Methane in Porous Ceramic Membrane Reactors. *Catal. Today* **2003**, 82, 255.
- (25) Amin, N. A. S.; Pheng, S. E. Influence of process variables and optimization of ethylene yield in oxidative coupling of methane over Li/MgO catalyst. *Chem. Eng. J.* **2006**, 116, 187.
- (26) Nouralishahi, A.; Pahlavanzadeh, H.; Daryan, T. Determination of optimal temperature profile in an OCM plug flow reactor for the maximizing of ethylene production. *Fuel Process. Technol.* **2008**, 89, 667.
- (27) Yuen, C. C.; Aatmeeyata; Gupta, S. K.; Ray, A. K. Multi-objective Optimization of membrane Separation Modules Using Genetic Algorithm. *J. Membr. Sci.* **2000**, 176, 177.
- (28) Goldberg, D. E. *Genetic Algorithms in Search, Optimization, and Machine Learning*; Addison-Wesley: Reading, MA, 1989.
- (29) Deb, K. *Optimization for Engineering Design: Algorithms and Examples*; Prentice Hall: New Delhi, 1995.
- (30) Cheng, S.; Chen, H.; Cheng, H.; Chang, C.; Chen, Y. Multi-objective Optimization for Two Catalytic Membrane Reactors-Methanol Synthesis and Hydrogen Production. *Chem. Eng. Sci.* **2008**, 63, 1428.
- (31) Lafarga, D.; Santamaria, J.; Menendez, M. Methane Oxidative Coupling Using Porous Ceramic Membrane Reactors—I. Reaction Studies. *Chem. Eng. Sci.* **1994**, 49, 2005.
- (32) Lane, G. S.; Wolf, A. E. Methane Utilization by Oxidative Coupling I. A Study of Reactions in the Gas Phase during the Co-Feeding of Methane and Oxygen. *J. Catal.* **1988**, 113, 144.
- (33) Allawi, Z. M.; Gunn, D. J. Flow and Diffusion of Gases Through Porous Substrates. *AIChE J.* **1987**, 33, 766.
- (34) Wu, J. C. S.; Liu, P. K. T. Mathematical Analysis on Catalytic Dehydrogenation of Ethyl-benzene Using Ceramic Membranes. *Ind. Eng. Chem. Res.* **1992**, 31, 322.
- (35) Bhaskar, V.; Gupta, S. K.; Ray, A. K. Application of Multiobjective Optimization in Chemical Engineering. *Rev. Chem. Eng.* **2000**, 16, 1.
- (36) Srinivas, N.; Deb, K. Multi-objective Function Optimization Using Non-Dominated Sorting Genetic Algorithm. *J. Evol. Comput.* **1995**, 2, 221.
- (37) Kasat, R. B.; Gupta, S. K. Multi-objective Optimization of an Industrial Fluidized-bed Catalytic Cracking Unit (FCCU) Using Genetic Algorithm with Jumping Genes Operator. *Comput. Chem. Eng.* **2003**, 27, 1785.
- (38) Guria, C.; Bhattacharya, P. K. Multi-objective Optimization of Reverse Osmosis Desalination Units Using Different Adaptation of Non-dominated Sorting Genetic Algorithm (NSGA). *Comput. Chem. Eng.* **2005**, 29, 1977.

Received for review June 16, 2009

Revised manuscript received May 20, 2010

Accepted May 25, 2010

IE900971P